Journal Pre-proof

Photocatalytic degradation using ZnO for the treatment of RB 19 and RB 21 dyes in industrial effluents and mathematical modeling of the process

Jorge Rodrigues, Tahmasb Hatami, Jorge Marcos Rosa, Elias Basile Tambourgi, Lucia Helena Innocentini Mei

This is a PDF file of an article that has undergone enhancements after acceptance, such as the addition of a cover page and metadata, and formatting for readability, but it is not yet the definitive version of record. This version will undergo additional copyediting, typesetting and review before it is published in its final form, but we are providing this version to give early visibility of the article. Please note that, during the production process, errors may be discovered which could affect the content, and all legal disclaimers that apply to the journal pertain.

Photocatalytic degradation using ZnO for the treatment of RB 19 and RB 21 dyes in industrial effluents and mathematical modeling of the process

Jorge Rodrigues[a, 1], Tahmasb Hatami[a], Jorge Marcos Rosa[b], Elias Basile Tambourgi[a], Lucia Helena Innocentini Mei[a]

[a]School of Chemical Engineering, University of Campinas, São Paulo, 13083-862, Brazil

[b] School of Technology of SENAI "Antoine Skaf", Correia de Andrade Street, 03008-020, Brás, São Paulo, SP, Brazil

[1] Corresponding author, Email: jorgerodriguesufv@gmail.com , Tel: +55 19-3521-3808, Fax: +55 19-3521-3894

Graphical abstract
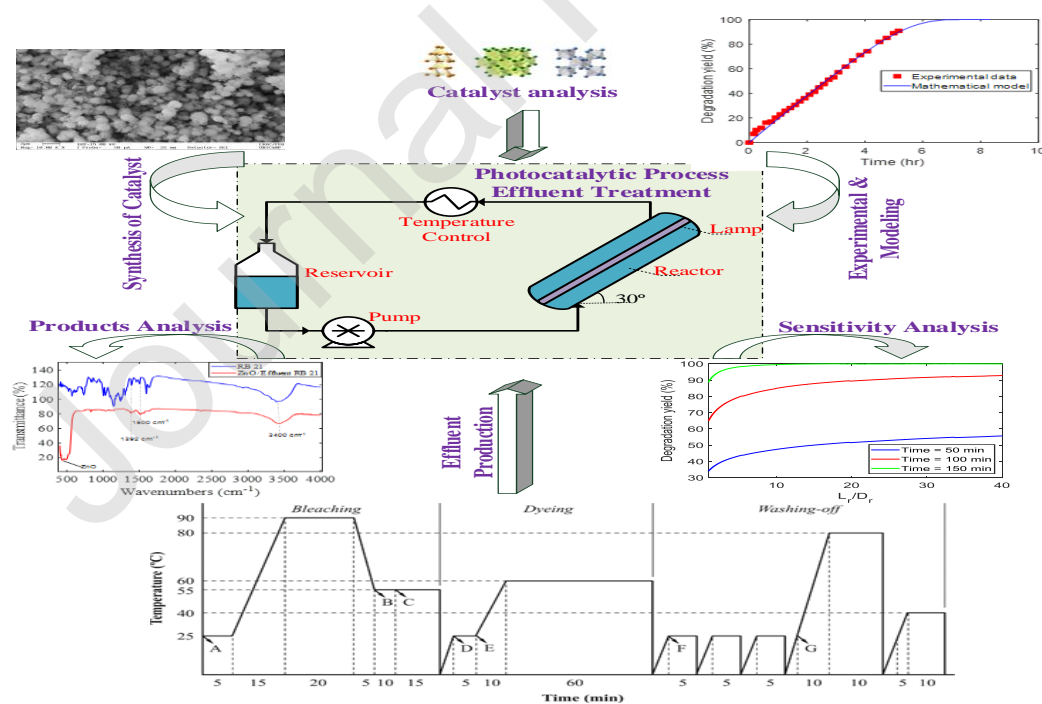
Highlights

- ZnO, ZnO-Ag and ZnO-Pd were synthesized for photodegradation of textile effluents.
- ZnO-Ag and ZnO-Pd degraded pure dye, but they did not degrade dyes in real effluents.
- ZnO degraded 100% of RB 19 and 91% of RB 21 during 5.8 h in the real effluents.
- The photocatalytic process was successfully modeled using the mass conservation law.
- Decreasing the dye concentration and catalyst size increased the degradation.

Abstract

ZnO-based catalysts impregnated with the metals Ag and Pd were synthesized for the photocatalytic degradation of two reactive dyes RB 19 and RB 21 in the textile effluents using an annular UV photoreactor. Among three synthesized catalysts, only the ZnO catalyst preserved the photodegradation of the dyes in the effluents. The density, mean particle diameter, surface area and porosity of the ZnO catalyst were 5550 kg/m^3, 1.19 $\times10^{-7}$ m, 16.830 m^2/g, and 0.1, respectively. It was found that the ZnO nanoparticles photodegradated the RB 19 and RB 21 by 100 and 91 % respectively over six hours. The photocatalytic degradation process was then modeled successfully based on the mass conservation law. The maximum photocatalytic degradation by the model can be obtained at the smaller catalyst size, lower initial dye concentration, and higher length per diameter ratio of the photocatalytic reactor.

Keywords: Photocatalytic degradation; Reactive Blue 19; Reactive Blue 21; ZnO nanoparticle; Mathematical modeling.

1. **Introduction**

The economy of developing countries, such as Brazil, depends heavily on several strategic industries, such as textiles (Amaral et al., 2018). However, the increase of this industrial activity is associated with major environmental problems, as textile effluents are of enormous chemical complexity due to the large number of unit operations required (Rosa et al., 2019).

There are several conventional methods for the treatment of textile effluents, which are considered expensive and difficult to maintain, such as biological systems (Das and Mishra, 2017), membranes (Hassan and Carr, 2018), filtration (Han et al., 2017, Jiang et al., 2018), and chemical treatment (Brik et al., 2004, Szpyrkowicz et al., 2001, Ahmadi et al., 2018). Advanced oxidation processes (AOP) are an interesting alternative, such as the beam treatment of effluents by photoelectrons (Tominaga et al., 2018, Borrely et al., 2016) and the use of ultraviolet radiation combined with metallic oxide catalysts (Wang, Han et al., 2019, Ding, Wang et al., 2018 Wang, Yu et al., 2019). As these materials can be obtained through low-cost technologies, they have been investigated in studies addressing photocatalytic reactions (Wang et al., 2019b, El-Bindary et al., 2019, Seong et al., 2019). Zn, Ti, Ag, Pd, Bi, Mo, W, V and Sn oxides are widely used in combination with other metallic oxides in photocatalytic applications (Wang et al., 2019c, Qin et al., 2019, Li et al., 2019, Zhu, Li et al., 2018, Zhang, Yu et al., 2019, Liu, Lin et al., 2018, Yang, Dong et al., 2019, Aramendía et al., 2008). Studies have demonstrated that ZnO is a more effective and suitable catalyst for the degradation of RB 19, RO 4 and RB 5 compared to TiO_2, SnO_2 and ZnS catalysts (Kansal et al., 2009, Lizama et al., 2002, Daneshvar et al., 2003). Table 1 shows some ZnO-based catalysts used in photocatalytic degradation processes. The table also reports the dyes, catalyst and dye concentrations, degradation time, required power and wavelength, and maximum degradation yield. The deposition of small quantities of

metals, such as palladium (Pd) and silver (Ag), which are very expensive, on the ZnO surface improves the catalytic properties (Seong et al., 2019, El-Bindary et al., 2019, Aramendía et al., 2008). A large number of studies have made considerable scientific contributions to the study of the photocatalytic degradation of pure pollutants (Calzada et al., 2019, Mohaghegh et al., 2015, Davar et al., 2015, Kansal et al., 2009). However, a survey of the literature revealed no papers on the degradation of pollutants in real effluents using photocatalyst oxides due to the complexity of wastewater (Rosa et al., 2019).

In this paper, we produce real effluents containing C.I. Reactive Blue 19 (RB 19) and C.I. Reactive Blue 21 (RB 21) dyes (Fig. 1) identical to those generated in textile processes involving the dyeing of cotton fabric (Rosa et al., 2019) and, for the first time, degrade the dyes with synthetized ZnO nanocatalysts impregnated with Pd and Ag.

After selecting the type of catalyst for the process, it is important to perform a sensitivity analysis and select the best operating conditions to achieve the optimal degradation rate. Several factors affect photocatalytic degradation, such as mean catalyst diameter, catalyst mass per volume of solution, initial pollutant concentration, diameter per length of the reactor, and UV light intensity. Examining the influence of these single factors and their interactions requires a large number of experiments, which increases the cost of research significantly. To overcome this limitation, the photocatalytic degradation process was modeled mathematically in the present study using mass conservation law to decrease the number of required experiments for the complete evaluation of pollutant degradation.

2. Materials and Methods

2.1. Synthesis of nanocatalysts

The ZnO catalyst was prepared by the co-precipitation method (Kasi and Seo, 2019, Nandi and Das, 2019, Bezerra et al., 2019) employing two solutions: one with zinc nitrate hexahydrate ($Zn(NO_3)_2 .6H_2O$) at 1.86 M as the source of Zn and another 0.5 M NaOH. These two solutions were slowly dripped into a beaker with initial volume of 40 mL of water, maintaining the pH close to 7 until complete solution consumption with the zinc salts. As the dropwise method promoted the mixing of the two solutions, hydroxylated zinc species were formed as precipitate. At the end of the drip method, the resulting system was aged at 40 °C for 24 h. The precipitate was vacuum filtered and washed to remove the liquid and sodium ions. The material was then dried at 40 °C for 12 h and calcined at 500 °C for 3 h.

2.2. Impregnation of ZnO with palladium and silver
2.2.1. Palladium (Pd)

A solution of palladium (II) chloride (Aldrich Chem., 99.99%) in concentrated hydrochloric acid at 100 °C was prepared with stirring for 45 min. Distilled water was added as the solution evaporated. After complete dissolution of the Pd^{2+} ions, the solution was added to a second solution prepared with the ZnO suspension (99% by mass in relation to Pd) in water at a temperature of 80 °C for 45 min. For metal impregnation of Pd to ZnO, the resulting mixture was then dried at 120 °C for 12 h and calcined in a furnace at 500 °C for 3 h. Finally, the obtained material (ZnO-Pd) was reduced in a furnace with hydrogen flow at 300 ℃ for 3 h.

2.2.2. Silver (Ag)

A solution was prepared by adding $Ag(NO_3)_2$ (PLAT-LAB 99.9 %) (1%) and ZnO (99%) to 10 mL of distilled water at 80 °C. The suspension was stirred for 45 minutes to impregnate the silver atoms on the surface of the ZnO and was then allowed to stand at

100 °C for the evaporation of water for 12 h. Next, the material was calcined at 500 °C

for 4 h and the oxide (ZnO-Ag) obtained was reduced in a hydrogen flow at 300 °C for

3 h.

2.3. Physical characterization of catalysts

The characteristics of the materials produced were determined using the Micromeritics

ASAP 2010 physical adsorption surface area analyzer (Austin, USA). Real density was

measured by helium gas pycnometry (PYC) (Micromeritics model: AccuPyc 1330,

Norcross, USA). The crystalline phases of the catalysts were identified by X-ray

diffraction (XRD) with the aid of the Philips Analytical X Ray equipment model

X´Pert-MPD (Almelo, The Netherlands) using monochromatic CuKα radiation (λ =

0.1541 nm) with a step of 0.02 (2θ). Nanoparticle size distribution was obtained using

ZetaSizer Nano S DLS (model - Malvern Instruments). The semi-quantification of the

elements found on the surface of the catalysts was performed using the X-ray

fluorescence PANalytical spectrometer (model: Axios 1KW).

2.4. Fourier-transform infrared (FTIR) spectroscopic and Total Organic Carbon (TOC) analysis

A spectrometer (Thermo Scientific mark, Model Nicolet 6700, Madison/USA) was used

in the transmittance mode in the SNAP-IN BASEPLATE accessory (KBr method) in

the range of 4000 to 400 cm^{-1} with a resolution of 4 cm^{-1} to analyze the dried catalyst,

dye, and effluent degradation products in the catalyst. Furthermore, these samples were

analyzed in terms of the carbon composition using catalytic combustion method by

TOC employed Shimadzu SSM-5000 Equipment.

2.5. Standard curves

Calibration standards were constructed with only the dyes (RB 19 and RB 21) using an

UV-Vis spectrophotometer for quantification based on the Beer-Lambert law for diluted

solutions. It was therefore possible to obtain the exact concentration of each dye in the effluents.

2.6. Adsorption

In the adsorption study, four solutions were prepared with various initial concentrations of industrials effluents (RB 19 and RB 21) in the range of 20 to 120 mg/L at a constant pH of 10. Next, a suspension containing 1.667 kg catalyst/m^3 of solution was prepared. These systems were maintained stirring at 1500 rpm in a dark environment at room temperature (27 °C). After 12 hours, an aliquot of each solution was removed, centrifuged to remove the catalyst in the system, and analyzed in a UV-Vis spectrophotometer (AJX 1900) with the maximum wavelength for each effluent (RB 21 - $\lambda_{max.}$= 624 nm and RB 19 - $\lambda_{max.}$= 595 nm) to calculate the equilibrium concentrations in the solid and liquid phases. These equilibrium concentrations were then used to obtain the parameters of the Langmuir isotherm model for use in the mathematical modeling.

As industrial applicability is the ultimate goal of any engineering research, the experiments in this study were carried out under the closest conditions to natural effluents, such as pH (~ 10) and room temperature. The amount of catalyst (1.667 kg/m^3 solution) was set based on preliminary tests in order to reduce the reaction time, as the initial dye concentration in the effluents (0.07 kg/m^3) was considerably higher than that found in most relevant publications listed in Table 4.

2.7. Production of effluents

The effluents were produced in the textile sector of the SENAI National Industrial Learning Service in São Paulo, Brazil. The composition of the chemical agents, time, and temperature for each step of the process are listed in Table 2 (Fig. 2). Two different

dyes were employed for the generation of two effluents: CI. Reactive Blue 21 (RB 21) and CI. Reactive Blue 19 (RB 19).

2.8. Auxiliaries

Sulfuric acid (98%), sodium hydroxide (98%), sodium metasilicate, sodium carbonate (98%), hydrogen peroxide (50%) and sodium chloride (98%) were supplied by Labsynth. Nonionic detergent and catalase enzyme were supplied by Golden Technology. The leveling agent was purchased from Archroma. All auxiliaries were used without previous purification.

2.9. Dyes

The RB 19 and RB 21 dyes were supplied by Archroma and were used without previous purification.

2.10. Operational montage of photochemical reaction system

Fig. 3 shows the reaction system used for the treatment of the effluents. This equipment contains a centrifugal pump (34 watts and 60 Hz), thermal controller, heat exchanger, mercury vapor lamp (made of quartz, 7.1 Watts, $250 < \lambda < 700$ nm), annular inclined reactor, and effluent reservoir. The pump was used for effluent recirculation at a flow rate of 1.64×10^{-5} m^3 s^{-1}. The reactor has an annular region between the inner wall and lamp surface. The inlet and outlet were tangentially confined to the inner wall, allowing the fluid to enter the reactor in a rotational movement, which maintains most of the catalyst in a circular motion during most of the treatment process. Thus, the reactor frame was mounted at a 30º inclination to the horizontal plane, as shown in Fig. 3A$_2$. The reactor was cooled with a stream of water to prevent the temperature from rising due to the heat generated by the UV-lamp. Dye concentrations were accurately monitored during the photocatalytic reactions. For such, aliquots were withdrawn with a

syringe (Fig. 3A$_1$), the catalyst nanoparticles were separated from the effluents using a centrifuge machine, and the dye concentration was determined by a UV-vis spectrophotometer. For a better understanding of the process, we limited the numerical simulation in Fig. 3A$_3$ according to the mass balance equations to determine the dye concentration profile in the solid and liquid stream.

2.11. Mathematical modeling and simulation

The concentration profiles in the photocatalytic reactor can be mathematically described by applying the mass balance conservation law for both the reactor and recycling line. The principle hypotheses for this purpose are spherical and mono-sized catalyst particles, a constant temperature, the Langmuir isotherm equilibrium between solution and catalyst, a constant reactor void fraction, and a first-order photocatalytic reaction of both pollutant concentration and UV light attenuation. The material balance in the reactor is described as follows:

$$\varepsilon_b \frac{\partial C_i}{\partial t} + a \frac{\partial q_i}{\partial t} = -U_r \frac{\partial C_i}{\partial z} - a k_{rxn} I q_i - \varepsilon_b R_{phot} \tag{1}$$

where C_i is the concentration of component i in the solution (kg/m^3), q_i is the concentration of component i at the catalyst surface (kg/m^2 of catalyst), U_r is the superficial fluid velocity inside the reactor (m/s), z is the axial axes (m), t is time (s), k_{rxn} is the photocatalytic reaction rate constant (m^2/J), I is the UV light intensity at the catalyst surface (W/m^2), and R_{phot} is the photolysis reaction rate (kg/m^3.s). Moreover

"a" is the specific surface area of catalyst in the reactor (m^2/m^3) that is calculated as follow:

$$a = \frac{6(1 - \varepsilon_{\mathrm{b}})}{d_{\mathrm{p}}} \qquad (2)$$

in which d_{p} is the catalyst diameter (m) and ε_{b} is the reactor porosity. Additionally, q_i and C_i are related to each other by the Langmuir isotherm model, as follows:

$$q_{\mathrm{i}} = \frac{q_{\max} b C_{\mathrm{i}}}{1 + b C_{\mathrm{i}}} \qquad (3)$$

in which $q_{\max}$ and b are the Langmuir isotherm constants. Placing q_i from Eq. (3) in Eq. (1), we get:

$$\left(\varepsilon_{\mathrm{b}} + a \frac{q_{\max} b}{(1 + b C_{\mathrm{i}})^2}\right) \frac{\partial C_{\mathrm{i}}}{\partial t} = -U_{\mathrm{r}} \frac{\partial C_{\mathrm{i}}}{\partial z} - a k_{\mathrm{rxn}} I \frac{q_{\max} b C_{\mathrm{i}}}{1 + b C_{\mathrm{i}}} - \varepsilon_{\mathrm{b}} R_{\mathrm{phot}} \qquad (4)$$

Similarly, applying the mass balance rule to the components in the recycling line, we get:

$$\frac{\partial c_{\mathrm{i}}}{\partial t} = -U_{\mathrm{e}} \frac{\partial c_{\mathrm{i}}}{\partial x} \qquad (5)$$

in which c_i is the concentration of component i in the recycling line (kg/m^3), U_{e} is the fluid velocity in the recycling line (m/s), and x is the axial axis (m).

The boundary and initial conditions for the above partial differential equations are as shown in Eq. (6):

$$\text{At } t = 0 \quad \Rightarrow \quad C_{\mathrm{i}} = c_{\mathrm{i}} = C_0$$
$$\text{At } z = 0 \ (x = L_e) \quad \Rightarrow \quad C_{\mathrm{i}} = c_{\mathrm{i}} \qquad (6)$$
$$\text{At } z = L_r \ (x = 0) \quad \Rightarrow \quad C_{\mathrm{i}} = c_{\mathrm{i}}$$

10

in which L_r (m) is the reactor length, L_e (m) is the length of recycling line, and C_{i0} (kmol/m^3) is the initial concentration of component i.

To solve the mathematical models (Eqs. (1) and (5)), the partial derivative of "C" with respect to "z" and the partial derivatives of "c" with respect to "x" were expanded using the finite difference method, whereas the partial derivatives of both "C" and "c" with respect to "t" were maintained unaltered. The two partial differential equations were converted to a set of ordinary differential equations, which were numerically solved using the ODE toolbox of the MATLAB software (MATLAB, 2017).

3. Results and Discussion

3.1. Experimental results

The semi-quantitative X-ray fluorescence analysis demonstrated that 1.123% of the Pd and 0.986% of the Ag were incorporated on the surface of ZnO nanoparticles, which consequently changed the crystallinity of the nanoparticles. The XRD analysis (Fig. 4) revealed that the nanoparticles only exhibited the crystallinity peaks of the hexagonal structure of the ZnO belonging to the wurtzite phase, according to the Inorganic Crystal Structure Database (code 01-089-1397). Based on the most intense peak area (2Θ equal to 36.25°), the ZnO-Ag sample had the highest crystallinity. Thus, the crystallinity of the other samples was normalized based on that of ZnO-Ag, which resulted in 81.3% for ZnO and 31.1% for ZnO-Pd. The impregnation of Ag atoms had less of an effect on the crystallinity of ZnO compared to Pd due to the preparation method. Employing heat and an acidic medium for palladium solubilization ($PdCl_2$) in the preparation method had a destructive effect on the crystallinity of the material (ZnO-Pd). In contrast, no impact was found on ZnO-Ag due to the solubilization of $Ag(NO_3)_2$ in distilled water with slight agitation. Fig. 4 displays the results of the ASAP analysis. According to the

11

classification of the International Union of Pure and Applied Chemistry, the catalysts

ZnO, ZnO-Ag and ZnO-Pd exhibit type H3 hysteresis and are characterized as low

porous materials formed by stacking particles, giving rise to slit-shaped platelets. These

three catalysts had BET areas of 16.269, 7.197, and 46.149 m^2/g and densities (by PYC)

of 5550, 57131, and 52579 kg/m^3, respectively. All catalysts exhibited very low

hysteresis and impregnation of the Pd nanoparticles, which caused a considerable

increase in the surface area of nanoparticles, making this material less dense, while the

Ag had a reverse effect. According to the ZetaSizer analysis, the nanoparticles

synthesized in the present study measured approximately 0.55 µm.

Fig. 5 shows the photodegradation and adsorption of the RB 21 dye in the solution with

an initial concentration of 0.70 kg/m^3 using the ZnO, ZnO-Ag and ZnO-Pd catalysts.

ZnO nanoparticles impregnated with Pd and Ag improved the removal rate of the dye

from the solution. ZnO-Ag achieved a large increase in the photocatalysis rate, whereas

ZnO-Pd achieved a high increase in adsorption due to the increase in the specific

surface area. However, when we investigated the degradation of the RB 19 and RB 21

dyes in the real effluents, neither catalyst (ZnO-Ag or ZnO-Pd) had catalytic activity,

which may be explained by the possible deactivation of catalytic sites by the adsorption

of the compounds rather than desorption in the solution.

ZnO was the only catalyst to preserve the photocatalytic characteristics of the

photodegradation of the RB 19 and RB 21 dyes in the effluents. Thus, we investigated

the possible chemical groups that remained at the end of the photocatalytic process on

the surface of the ZnO nanoparticles after the degradation of the dyes. We then

employed mathematical modeling to determine the best treatment conditions for the pollutants.

3.2. FTIR and TOC: analysis of chemical groups on surface of catalyst and carbon composition

Fig. 6A shows the FTIR spectrum of the ZnO nanoparticles, the absorption bands characteristic of ZnO around 450-500 cm^{-1} and the presence of surface hydroxyls in the 3400 cm^{-1} region. Fig. 6B shows an increase in hydroxylated compounds at approximately 3400 cm^{-1} and simultaneously in the 3220-3450 cm^{-1} range due to the NH stretching of aromatic amines in the reaction products with the effluent containing RB 19 (Matthews et al., 2009). However, this effect was not found in the treatment of the effluent with RB 21 (Fig. 6C). The dyes used in this study have several similar organic groups with characteristic vibration bands in the range of 1640 to 1000 cm^{-1}. Fig. 6B and 6C show the bands after the treatment of the effluents resulting from the mixing between the ZnO and the products of the reaction medium due to the degradation of RB 19 and RB 21, respectively. These spectra indicate a considerable reduction in the organic compounds previously observed in the dye powders. Less complex organic compounds are found after the reactions compared to those previously analyzed in the dyes.

Moreover, many chemical groups were no longer present in the reaction products of the effluents with RB 21, having become impregnated on the ZnO (ZnO/effluent RB 21), as seen in Fig. 6C. Few vibrational modes remained, occurring for the stretching at 1500 cm^{-1} associated with a possible C=C in aromatic groups and at 1392 cm^{-1} associated with dimethyl groups. However, other chemical groups were maintained, such as those found in the reaction products of the effluents with RB 19 that were impregnated on the ZnO (ZnO/effluent RB 19), as seen in Fig. 6B, occurring for the stretching at around

13

1637 cm^{-1} associated with C=C in alkenes, 1560 cm^{-1} associated with O=N=O, between 1450 and 1200 cm^{-1} associated with C-O of phenol and 1047 cm^{-1} associated with S=O (Bilal et al., 2018, Verma et al., 2019, Mishra et al., 2019, Kaur et al., 2019).

TOC analysis was performed based on this comment and showed that ZnO was free of organic carbon before the treatment of the effluent, whereas ZnO-RB19 and ZnO-RB21 had total organic carbon of 0.53% and 1.01%, respectively. These results are consistent, since the initial dye concentrations in the two effluents were the same (0.07 kg/m3) and the RB 21 dye contains the phthalocyanine group, which has more carbons than the anthraquinones in the RB 19 dye (De La Torre et al., 2002, Moussavi et al., 2009). Thus, the reduction in the organic charge discussed in the FTIR analysis corroborates the elimination of large amounts of organic charge, which indicates the formation of carbon monoxide and dioxide during the photocatalytic process.

3.3. Modeling and simulation of dye photodegradation in effluents using ZnO nanoparticles

Prior to comparing the results of the model of photocatalytic degradation and the experimental data, it is necessary to calculate the Langmuir isotherm constants (q_{max} and b) and the photolysis reaction rate ($R_{photolysis}$) as well as multiply the photocatalytic reaction rate constant and the UV light intensity at the catalyst surface ($k_{rxn}I$). Using the curve fitting toolbox of the MATLAB software, the Langmuir isotherm model fits the experimental adsorption data of both dyes well, with a coefficient of determination of 0.998. The q_{max} and b values obtained from this fitting are given in Table 3.

Moreover, the experimental data of photolysis degradation for both dyes changed linearly with time over a period of 320 min, which means that photolysis degradation is zero order with respect to the dye concentration. The photolysis reaction rates are also displayed in Table 3. This table presents the numerical values of the initial concentration (C_o) of the dyes, catalyst size (d_p), length (L_r) and diameter of the reactor (D_r), length (L_l) and diameter (D_l) of the UV lamp, length (L_e) and equivalent diameter (D_e) of the recycling line, specific surface area of the catalyst (a), and superficial fluid velocity in the reactor (U_r) and in the recycling line (U_e).

Fig. 7 represents the photocatalytic degradation of RB 21 and RB 19 using ZnO nanoparticles in the photocatalytic reactor. The results of the model are in excellent agreement with the experimental data, especially for RB 21. Thus, the model assumptions are more reliable for RB 21 than RB 19. Based on the model results, 100% degradation is achieved in 6.8 h for RB 21 and 5.8 h for RB 19. This difference in photocatalytic rates is mainly due to the chemical structures of the dyes (Fig. 1) and their respective hydrolysates produced in the effluents (Nechwatal, Nicolai et al., 1999, Thomsen 1994).

After validation, the model was used to investigate the effects of the initial dye concentration, catalyst size, and length per diameter ratio of the photocatalytic reactor on degradation. It is assumed that the photocatalytic reaction rate remains constant. As seen in Fig. 8A and 8B, the percentage of photocatalytic degradation increases considerably with the decrease in both catalyst size and initial pollutant concentration. The former impact is due to the increase in the specific surface area of the catalyst with the decrease in catalyst size, while the latter is due to the increase in the reaction sites per pollutant molecule. Fig. 8C and 8D show that degradation increases considerably

15

with the length per diameter ratio of the reactor from 1 to 8. However, a further increase of this ratio does not notably improve the yield. For the photocatalytic lab reactor used in the present study, this ratio is 7.78, which demonstrates the optimum designing of the reactor based on the model findings. It is noteworthy that the lamp diameter in Fig. 8E and 8F is constant, but the length changes with the change in reactor length to cover the entire reactor. Thus, increasing the length per diameter ratio of the reactor has two opposite effects on the degradation rate. On the one hand, it increases the average UV intensity due to the increase in lamp length, which consequently enhances the degradation rate (dominant effect). On the other hand, it decreases the average residence time of the fluid in the reactor due to the reduction in the reactor volume, which has a negative impact on the degradation rate. Another point that can be extracted from Fig. 8 is that the trends of the degradation curves are approximately the same for different degradation times.

This paper shows that many of the catalysts used for the photodegradation of dyes in their pure form do not function for pollutants in real effluents. As seen in Table 4, most studies in the literature investigate the degradation of pure dyes and use high-power radiation to achieve a high degradation rate. In this work, we employed low-power UV-visible radiation and ZnO nanoparticles to degrade nearly all the dyes in the effluent.

4. Conclusion

The following are the main conclusions drawn from this paper:

1- The ZnO nanoparticles exhibited considerable catalytic activity for the photodegradation of the RB 19 and RB 21 dyes in the effluents generated: 100 and 91 % respectively.

16

2- The ZnO-Ag and ZnO-Pd catalysts exhibited high photocatalytic activity regarding the degradation of the dyes in pure solutions (95%) but did not achieve any degradation when used to degrade dyes in real effluents.

3- The surface area of the ZnO-Ag nanoparticles was smaller compared to ZnO, leading to an improvement in photocatalytic performance during the degradation of the pure dyes. However, ZnO-Pd had the opposite effect due to a strong increase in the adsorption rate.

4- The FTIR analysis showed that the amount of hydroxylated and amine-associated aromatic compounds increased in the effluent with RB 19. However, *a* small variety was found in the composition of products obtained through the degradation of the effluent containing RB 21.

5- The minimum mean absolute deviation of the model from the experimental degradation data was less than 1.5% and maximum deviation was around 7%.

6- The model showed that reductions in pollutant concentration and catalyst size led to an increase in the percentage of photocatalytic degradation.

Declarations of interest

None

Conflict of Interest and Authorship Conformation Form

All authors have participated in (a) conception and design, analysis and interpretation of the data; (b) drafting the article and revising it critically for important intellectual content; and (c) approval of the final version. This manuscript has not been submitted to, nor is under review at, another journal or other publishing venue.

Acknowledgements

References

Ahmadi, S., Mohammadi, L., Igwegbe, C. A., Rahdar, S., Banach, A. M., 2018. Application of response surface methodology in the degradation of Reactive Blue 19 using H_2O_2/MgO nanoparticles advanced oxidation process. Int. J. Ind. Chem. 9(3), 241-253.

Al-Anbari, R., Al Obaidy, A. H., Abed, E., 2017. Solar Photocatalytic of Reactive Blue Dye in Aqueous Suspension of V_2O_5. J. Eng. Technol. 35, 1-8.

Alam, U., Shah, T. A., Khan, A., Muneer, M., 2019. One-pot ultrasonic assisted sol-gel synthesis of spindle-like Nd and V codoped ZnO for efficient photocatalytic degradation of organic pollutants. Sep. Purif. Technol. Separation. 212, 427-437.

Ali, A., Gul, A., Ambreen, S., Phull, A. R., Zia, M., 2018. Effective photocatalysis of direct dyes under sunlight by silver, iron, and zinc nanoparticles doped on cotton. J. Environ. Chem. Eng. 6(5), 5915-5919.

Amaral, M. C. d., Zonatti, W. F., Silva, K. L. d., Karam Junior, D., Amato Neto, J., Baruque-Ramos, J., 2018. Industrial textile recycling and reuse in Brazil: case study and considerations concerning the circular economy. Manag. Prod. 25(3), 431-443.

Aramendía, M., Borau, V., Colmenares, J., Marinas, A., Marinas, J., Navío, J., Urbano, F., 2008. Modification of the photocatalytic activity of Pd/TiO_2 and Zn/TiO_2 systems through different oxidative and reductive calcination treatments. Appl. Catal., B. Appl. Clay Sci. 80(1-2), 88-97.

Atrak, K., Ramazani, A., Taghavi Fardood, S., 2019. Green synthesis of $Zn_{0.5}Ni_{0.5}AlFeO_4$ magnetic nanoparticles and investigation of their photocatalytic activity for degradation of reactive blue 21 dye. Environ. Technol. 1-11.

Bahreini, Z., Heydari, V., Hekmat, A. N., Taheri, M., Vahid, B., Moradkhannejhad, L., 2016. A comparative study of photocatalytic degradation and mineralisation of an azo dye using supported and suspended nano-TiO_2 under UV and sunlight irradiations. Pigm. Resin Technol. 45(2), 119-125.

Bezerra, J., Matos, R., Zucolotto, B., Pedra, P., Ferreira, N., 2019. Effects of different complexing agents on the physical properties of ZnO nanoparticles. J. Mater. Sci. Technol. 35(2), 231-239.

Bilal, M., Rasheed, T., Iqbal, H. M. N., Li, C., Wang, H., Hu, H., Zhang, X., 2018. Photocatalytic degradation, toxicological assessment and degradation pathway of C.I. Reactive Blue 19 dye. Chem. Eng. Res. Des. 129, 384-390.

Borrely, S. I., Morais, A. V., Rosa, J. M., Badaró-Pedroso, C., da Conceição Pereira, M., Higa, M. C., 2016. Decoloration and detoxification of effluents by ionizing radiation. Radiat. Phys. Chem. 124, 198-202.

Brik, M., Chamam, B., Schöberl, P., Braun, R., Fuchs, W., 2004 Effect of ozone, chlorine and hydrogen peroxide on the elimination of colour in treated textile wastewater by MBR. Water Sci. Technol. 49, 299-303.

Calzada, L. A., Castellanos, R., García, L. A., Klimova, T. E., 2019. TiO_2, SnO_2 and ZnO catalysts supported on mesoporous SBA-15 versus unsupported nanopowders in photocatalytic degradation of methylene blue. Micropor. Mesopor. mat. 285, 247-258.

Daneshvar, N., Salari, D., Khataee, A. R., 2003. Photocatalytic degradation of azo dye acid red 14 in water: investigation of the effect of operational parameters. J. Photochem. Photobiol. A Chem. 157(1), 111-116.

Das, A., Mishra, S., 2017. Removal of textile dye reactive green-19 using bacterial consortium: process optimization using response surface methodology and kinetics study. J. Environ. Chem. Eng. 5(1), 612-627.

Davar, F., Majedi, A., Mirzaei, A., 2015. Green synthesis of ZnO nanoparticles and its application in the degradation of some dyes. Am. Ceram. Soc. 98(6), 1739-1746.

De la Torre, G., Torres T., 2002. Synthetic advances in phthalocyanine chemistry. J. Porphyr. Phthalocyanines. 6 (04), 274-284.

De la Torre, G. and T. Torres (2002). "Synthetic advances in phthalocyanine chemistry." Journal of Porphyrins and Phthalocyanines 6(04): 274-284.

Ding, K., Wang, W., Yu, D., Gao, P., Liu, B., 2018. Facile formation of flexible Ag/AgCl/polydopamine/cotton fabric composite photocatalysts as an efficient visible-light photocatalysts. Appl. Surf. Sci. 454, 101-111.

El-Bindary, A., El-Marsafy, S., El-Maddah, A., 2019. Enhancement of the photocatalytic activity of ZnO nanoparticles by silver doping for the degradation of AY 99 contaminants. J. Mol. Struct. 1191, 76-84.

Fan, J., Yu, D., Wang, W., Liu, B., 2019. The self-assembly and formation mechanism of regenerated cellulose films for photocatalytic degradation of CI Reactive Blue 19. Cellulose. 26(6), 3955-3972.

Fardood, S. T., Golfar, Z., Ramazani, A., 2017. Novel sol–gel synthesis and characterization of superparamagnetic magnesium ferrite nanoparticles using tragacanth gum as a magnetically separable photocatalyst for degradation of reactive blue 21 dye and kinetic study. J. Mater. Sci. 28(22), 17002-17008.

Han, G., Feng, Y., Chung, T.-S., Weber, M., Maletzko, C., 2017. Phase inversion directly induced tight ultrafiltration (UF) hollow fiber membranes for effective removal of textile dyes. J. Environ. Sci. Technol. 51(24), 14254-14261.

Hassan, M. M., Carr, C. M., 2018. A critical review on recent advancements of the removal of reactive dyes from dyehouse effluent by ion-exchange adsorbents. Chemosphere. 209, 201-219.

Jiang, M., Ye, K., Deng, J., Lin, J., Ye, W., Zhao, S., Van der Bruggen, B., 2018. Conventional ultrafiltration as effective strategy for dye/salt fractionation in textile wastewater treatment. J. Environ. Sci. Technol. 52(18), 10698-10708.

Kalikeri, S., Kamath, N., Gadgil, D. J., Kodialbail, V. S., 2018. Visible light-induced photocatalytic degradation of Reactive Blue-19 over highly efficient polyaniline-TiO_2 nanocomposite: a comparative study with solar and UV photocatalysis. Environ. Sci. Pollut. Res. 25(4), 3731-3744.

Kansal, S. K., Kaur, N., Singh, S., 2009. Photocatalytic degradation of two commercial reactive dyes in aqueous phase using nanophotocatalysts. Nanoscale Res. Lett. 4(7), 709.

Kasi, G., Seo, J., 2019. Influence of Mg doping on the structural, morphological, optical, thermal, and visible-light responsive antibacterial properties of ZnO nanoparticles synthesized via co-precipitation. J. Mat Sci. Eng. c mater. 98, 717-725.

Kaur, B., Chand, S., Malik, A. K., Dhaliwal, K. S., Younis, S. A., Kim, K.-H., 2019. One-pot three-component synthesis of α-amino nitriles using ZnO as a heterogeneous, reusable, and eco-friendly catalyst. J. Clean. Prod. 234, 329-339.

Khan, M. A. N., Siddique, M., Wahid, F., Khan, R., 2015. Removal of reactive blue 19 dye by sono, photo and sonophotocatalytic oxidation using visible light. Ultrason. Sonochem. 26, 370-377.

Li, B., Lai, C., Xu, P., Zeng, G., Huang, D., Qin, L., Huang, F., 2019. Facile synthesis of bismuth oxyhalogen-based Z-scheme photocatalyst for visible-light-driven pollutant removal: Kinetics, degradation pathways and mechanism. J. Clean. Prod. 225, 898-912.

Lin, L., Yu, D., Wang, W., Gao, P., Bu, K., Liu, B., 2016. Preparation of $BiVO_4/Bi_2WO_6$/multi-walled carbon nanotube nanocomposites for enchaning photocatalytic performance. Mater. Lett. 185, 507-510.

Liu, B., Lin, L., Yu, D., Sun, J., Zhu, Z., Gao, P., Wang, W., 2018. Construction of fiber-based $BiVO_4/SiO_2$/reduced graphene oxide (RGO) with efficient visible light photocatalytic activity. Cellulose 25(2), 1089-1101.

Lizama, C., Freer, J., Baeza, J., Mansilla, H. D., 2002. Optimized photodegradation of Reactive Blue 19 on TiO_2 and ZnO suspensions. Catal. Today. 76(2), 235-246.

Matthews, R. D., Bottomley, L. A., Pavlostathis, S. G., 2009. Palladium-catalyzed hydrogen reduction and decolorization of reactive phthalocyanine dyes. Desalination. 248(1-3), 816-825.

Maučec, D., Šuligoj, A., Ristić, A., Dražić, G., Pintar, A., Tušar, N. N., 2018. Titania versus zinc oxide nanoparticles on mesoporous silica supports as photocatalysts for removal of dyes from wastewater at neutral pH. Catal. Today. 310, 32-41.

Mishra, S., Mohanty, P., Maiti, A., 2019. Bacterial mediated bio-decolourization of wastewater containing mixed reactive dyes using jack-fruit seed as co-substrate: Process optimization. J. Clean. Prod. 235, 21-33.

Modwi, A., Taha, K. K., Khezami, L., Bououdina, M., Houas, A., 2019. Silver decorated Cu/ZnO photocomposite: efficient green degradation of malachite. J. Mater. Sci. 30, 3629-3638.

Mohaghegh, N., Rahimi, E., Gholami, M. R., 2015. $Ag_3PO_4/BiPO_4$ p-n heterojunction nanocomposite prepared in room-temperature ionic liquid medium with improved photocatalytic activity. Mat. Sci. Semicon. Proc. 39, 506-514.

Moussavi, G., Mahmoudi M., 2009. Removal of azo and anthraquinone reactive dyes from industrial wastewaters using MgO nanoparticles. J. Hazard. Mater. 68(2), 806-812.

Moradi, S., Taghavi Fardood, S., Ramazani, A., 2018. Green synthesis and characterization of magnetic $NiFe_2O_4$@ZnO nanocomposite and its application for photocatalytic degradation of organic dyes. J. Mater. Sci. 29(16), 14151–14160.

Moradnia, F., Ramazani, A., Fardood, S. T., Gouranlou, F., 2019. A novel green synthesis and characterization of tetragonal-spinel $MgMn_2O_4$ nanoparticles by tragacanth gel and studies of its photocatalytic activity for degradation of reactive blue 21 dye under visible light. Mater. Res. Express. 6(7), 075057.

Nandi, P., Das, D., 2019. Photocatalytic degradation of Rhodamine-B dye by stable ZnO nanostructures with different calcination temperature induced defects. Appl Surf Sci. 465, 546-556.

Nechwatal, A., Nicolai, M., Mieck, K. P., 1999. Use of absorbers based on starch for the effluent treatment of dyeing liquors. Starch-Starke, 51(8- 9), 286-293.

Pardiwala, J., Patel, F., Patel, S., 2016. Synthesis of a spinel catalyst by mechanochemical reaction for the degradation of RB 21 dye. J. Environ. Res. Dev. 11(2), 250.

Qin, Y., Li, H., Lu, J., Dong, H., Ma, C., Liu, X., Yan, Y., 2019. Synthesis of QDs self-modified Bi_2MoO_6/$Bi_4Ti_3O_{12}$ photocatalysts via controlling charge unidirectional flow for effective degradation of organic pollutants. J. Mol. Liq. 286, 110919.

Rosa, J. M., Garcia, V. S., Boiani, N. F., Melo, C. G., Pereira, M. C., Borrely, S. I., 2019. Toxicity and environmental impacts approached in the dyeing of polyamide, polyester and cotton knits. J. Environ. Chem. Eng. 7(2), 102973.

Seong, S., Park, I.-S., Jung, Y. C., Lee, T., Kim, S. Y., Park, J. S., Ahn, J., 2019. Synthesis of Ag-ZnO core-shell nanoparticles with enhanced photocatalytic activity through atomic layer deposition. Mater. Design. 177, 107831.

Szpyrkowicz, L., Juzzolino, C., Kaul, S. N., 2001. A comparative study on oxidation of disperse dyes by electrochemical process, ozone, hypochlorite and fenton reagent. Water Res. 35(9), 2129-2136.

Tanji, K., Navio, J., Naja, J., Hidalgo, M., Chaqroune, A., Jaramillo-Páez, C., Kherbeche, A., 2019. Extraordinary visible photocatalytic activity of a $Co_{0.2}Zn_{0.8}$ system studied in the Remazol BB oxidation. J. Photochem. Photobiol. A Chem. 382, 111877.

Thomsen, B., 1994. The washing out of hydrolysed dyestuff - a permanent challenge. Melliand. Textilber. 75, 220-222.

Tominaga, F. K., dos Santos Batista, A. P., Teixeira, A. C. S. C., Borrely, S. I., 2018. Degradation of diclofenac by electron beam irradiaton: Toxicitiy removal, by-products identification and effect of another pharmaceutical compound. J. Environ. Chem. Eng. 6(4), 4605-4611.

Verma, A., Soni, R. K., Teotia, M., 2019. Prevention of poly(vinyl chloride) degradation through organic terephthalamides generated from poly(ethylene terephthalate) waste. J. Appl. Polym. Sci. 136(40).

Wang, L., Li, Z., Chen, J., Huang, Y., Zhang, H., Qiu, H., 2019. Enhanced photocatalytic degradation of methyl orange by porous graphene/ZnO nanocomposite. Environ. Pollut. 801-811.

Wang, P., Ng, D. H., Zhou, M., Li, J., 2019. Freely standing MgAl-layered double hydroxides nanosheets and their derived metal oxides on g-C_3N_4 thin-layer designed for obtaining synergic effect of adsorption and photocatalysis. Appl. Clay Sci. 178, 105131.

Wang, T., Tang, T., Gao, Y., Chen, Q., Zhang, Z., Bian, H., 2019. Hydrothermal preparation of Ag-TiO_2-reduced graphene oxide ternary microspheres structure composite for enhancing photocatalytic activity. Physica E. 112, 128-136.

Wang, Y., Yu, D., Wang, W., Gao, P., Zhang, L., Zhong, S., Liu, B., 2019. The controllable synthesis of novel heterojunction $CoO/BiVO_4$ composite catalysts for enhancing visible-light photocatalytic property. Colloids Surf. A Physicochem Eng Asp. 578, 123608.

Wang, W., Han, Q., Zhu, Z., Zhang, L., Zhong, S., Liu, B., 2019. Enhanced photocatalytic degradation performance of organic contaminants by heterojunction photocatalyst $BiVO_4/TiO_2/RGO$ and its compatibility on four different tetracycline antibiotics. Adv. Powder. Technol. 30, 1882–1896.

Wang, Z., Xuan, J., Liu, B., He, J., 2015. Photocatalytic degradation of CI reactive blue 19 by using novel nano $BiVO_4$-coated cotton fabric. J. Ind. Text. 44(6), 868-883.

Yang, R., Dong, F., You, X., Liu, M., Shan, Z., Lishan, Z., Liu, B., 2019. Facile synthesis and characterization of interface charge transfer heterojunction of Bi_2MoO_6 modified by Ag/AgCl photosensitive material with enhanced photocatalytic activity. Mater. Lett. 252, 272-276.

Yu, C., Tong, Z., Li, S., Yin, Y., 2019. Enhancing the photocatalytic activity of ZnO by using tourmaline. Mater. Lett. 240, 161-164.

Zhang, H., Yu, D., Wang, W., Gao, P., Bu, K., Zhang, L., Zhong, S., Liu, B., 2019. Multiple heterojunction system of $Bi_2MoO_6/WO_3/Ag_3PO_4$ with enhanced visible-light photocatalytic performance towards dye degradation. Adv. Powder. Technol. 30 1910-1919.

Zhu, Z., Li, Y., Wang, C., Liang, L., Yu, D., Sun, J., Gao, P., Liu, B., 2018. Facile synthesis and characterization of $Bi_2MoO_6/Ag_3PO_4/RGO$ composites with enhanced visible-light-driven photocatalytic activity. Mater. Lett. 227: 296-300.

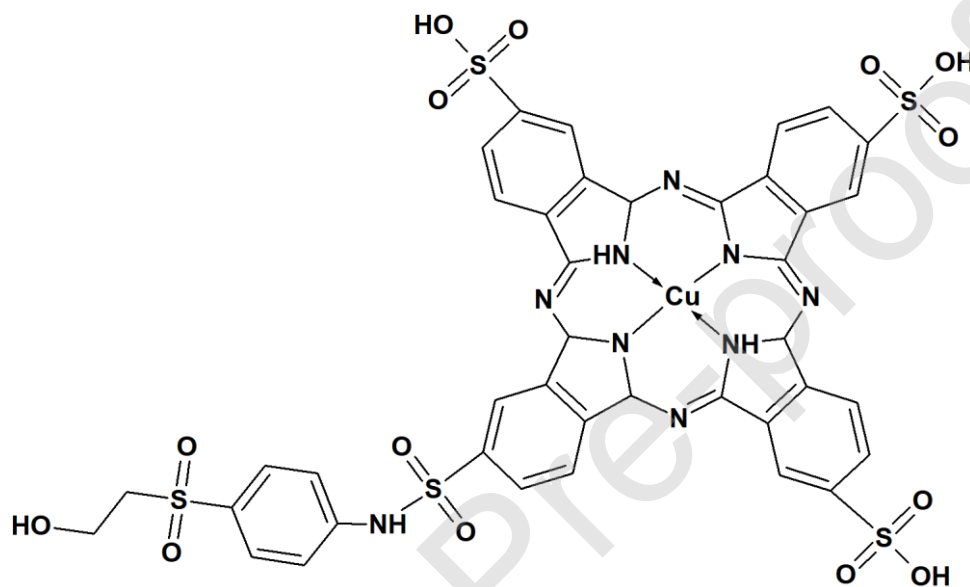**RB 19**
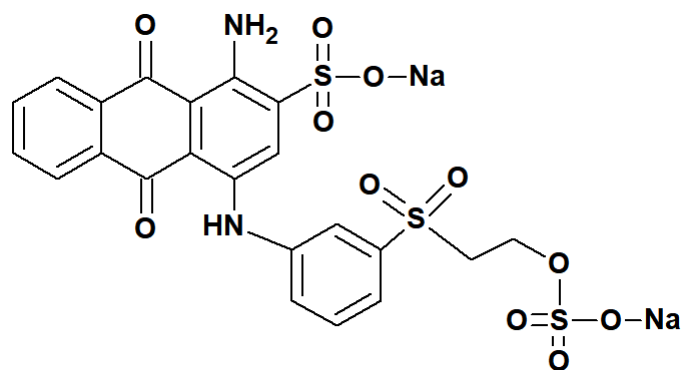
RB 21

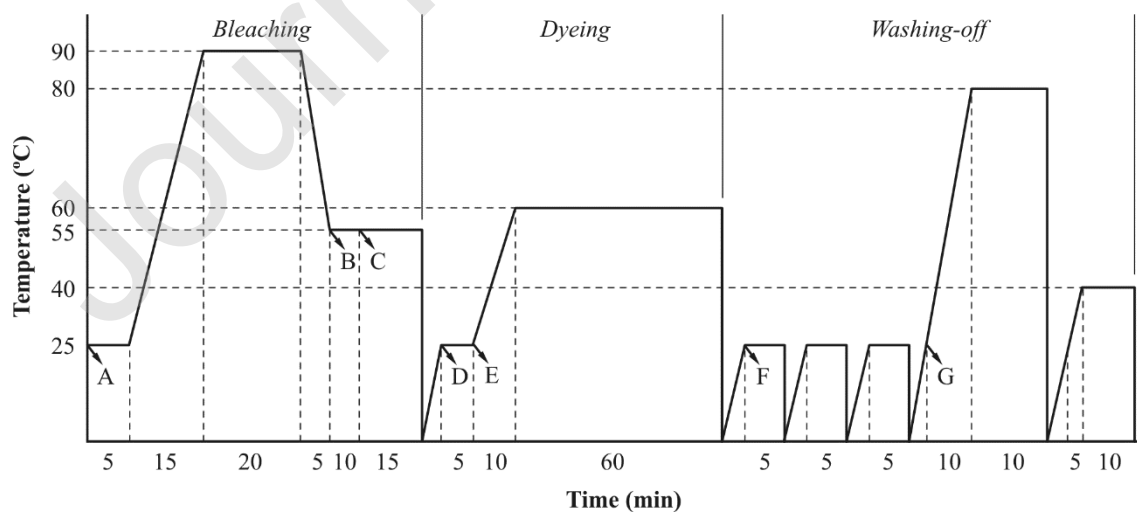**Figure 1-** Molecular structure of the dyes.
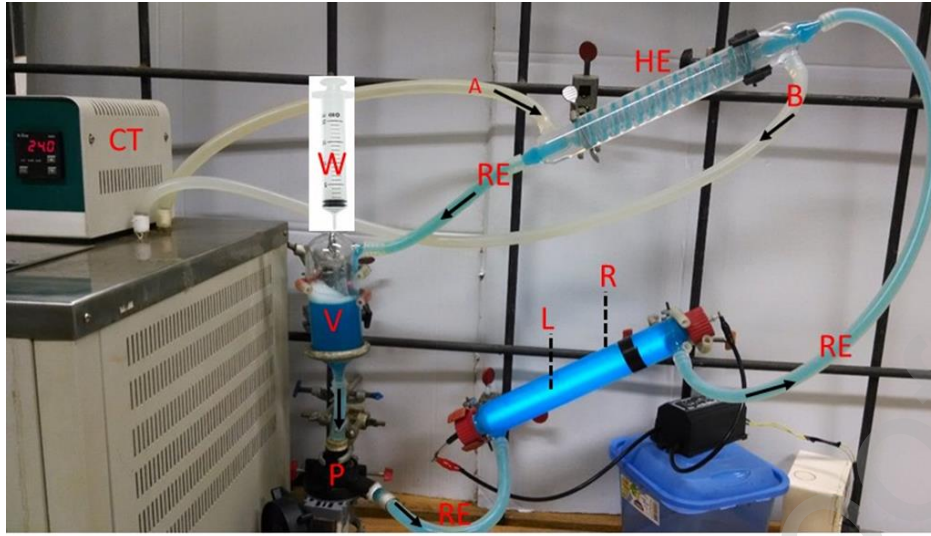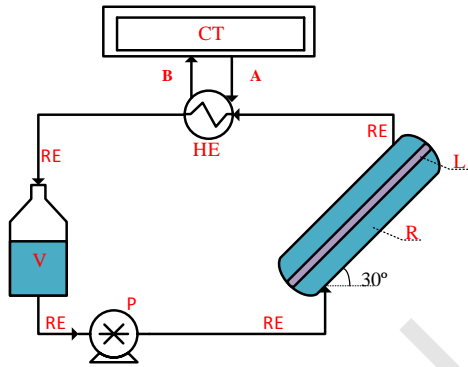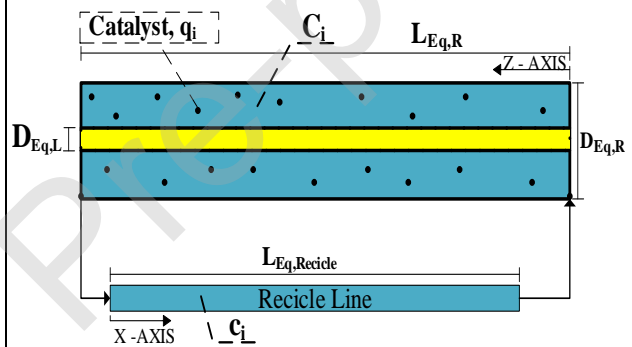

Figure 2- Dyeing procedure of the cotton processing.

Figure 3 – Schematic diagram of PCR (W: Aliquot Removal, CT:Thermal Control, HE: Heat Exchanger, RE: Recycling line, L: Lamp, R: Reactor, A: Cooling Water Inlet, B: Cooling Water Outlet, V: Effluent Reservoir, A_3: Simplified PCR process and recycling line for the mathematical modeling).
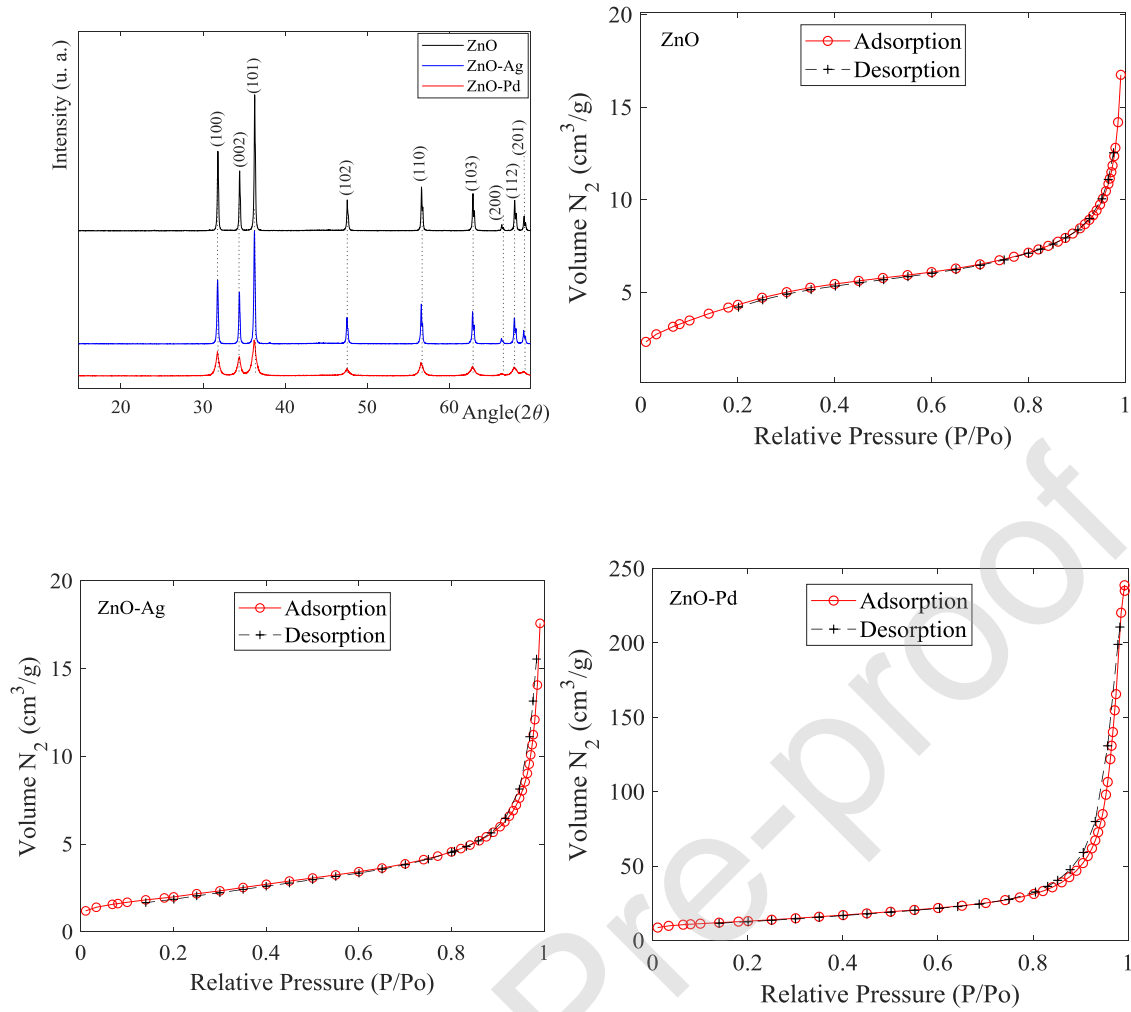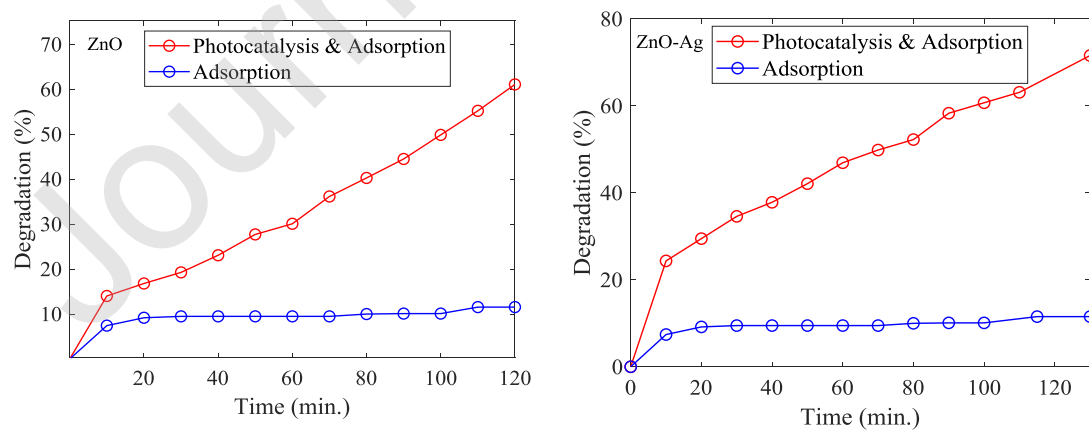
Figure 4 – XRD and ASAP analysis of catalysts.
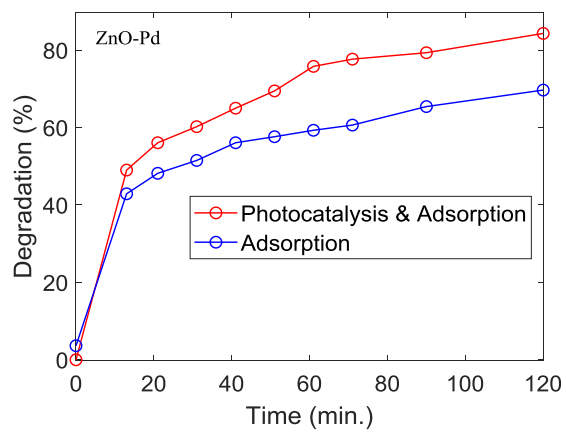
Figure 5 – Photocatalytic degradation of RB 21.
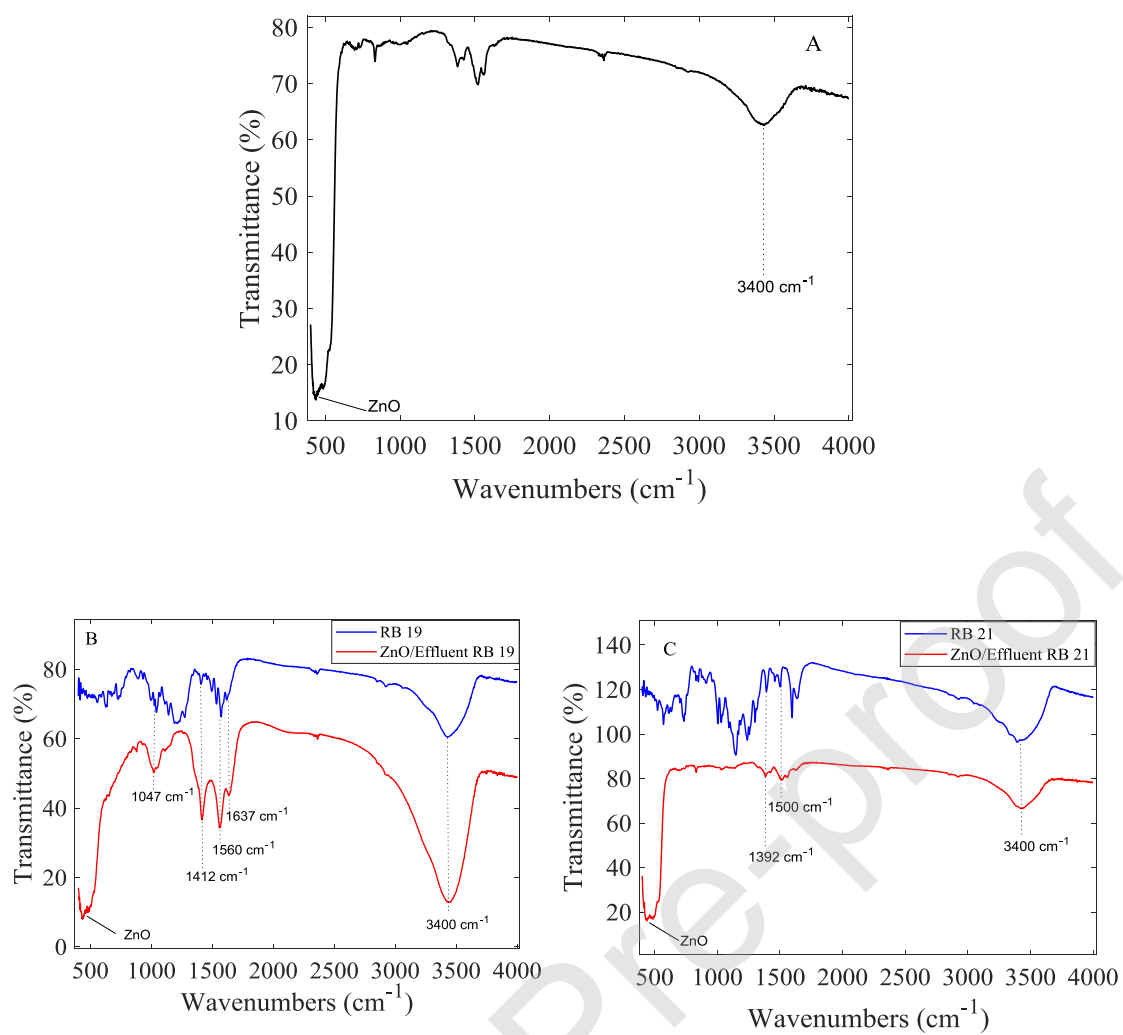
Figure 6 - FTIR spectra of pure dyes employed in the produced effluent, and reaction products (ZnO/Effluent) impregnated with ZnO.
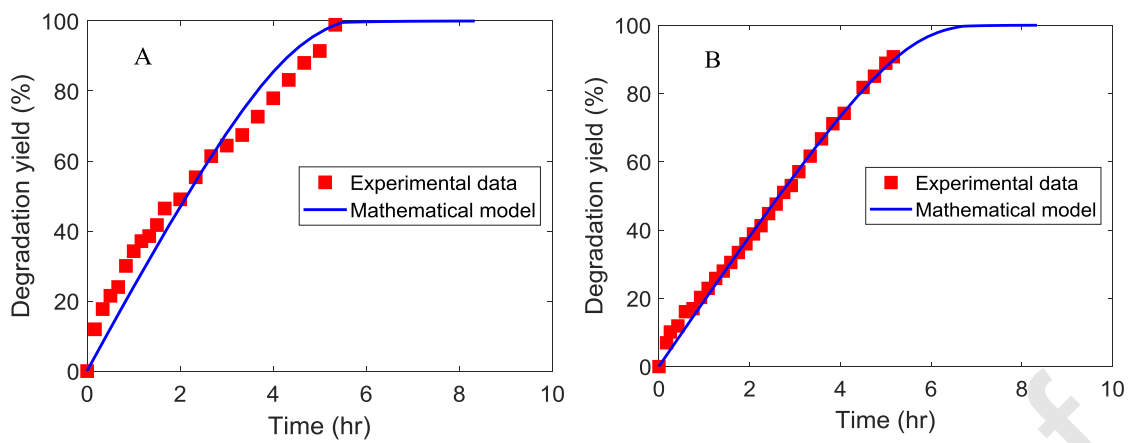
Figure 7 - Comparison of the model and experimental data for photodegradation of (A) RB 19 and (B) RB 21.

Figure 8 - Influences of initial dyes concentration (A: RB 19 and B: RB 21), catalyst diameter (C: RB 19 and D: RB 21), and length per diameter ratio of PCR (E: RB 19 and F: RB 21) on the degradation yield for various degradation times.

Table 1 - Comparison total photocatalytic degradation in present study and relevant publications.

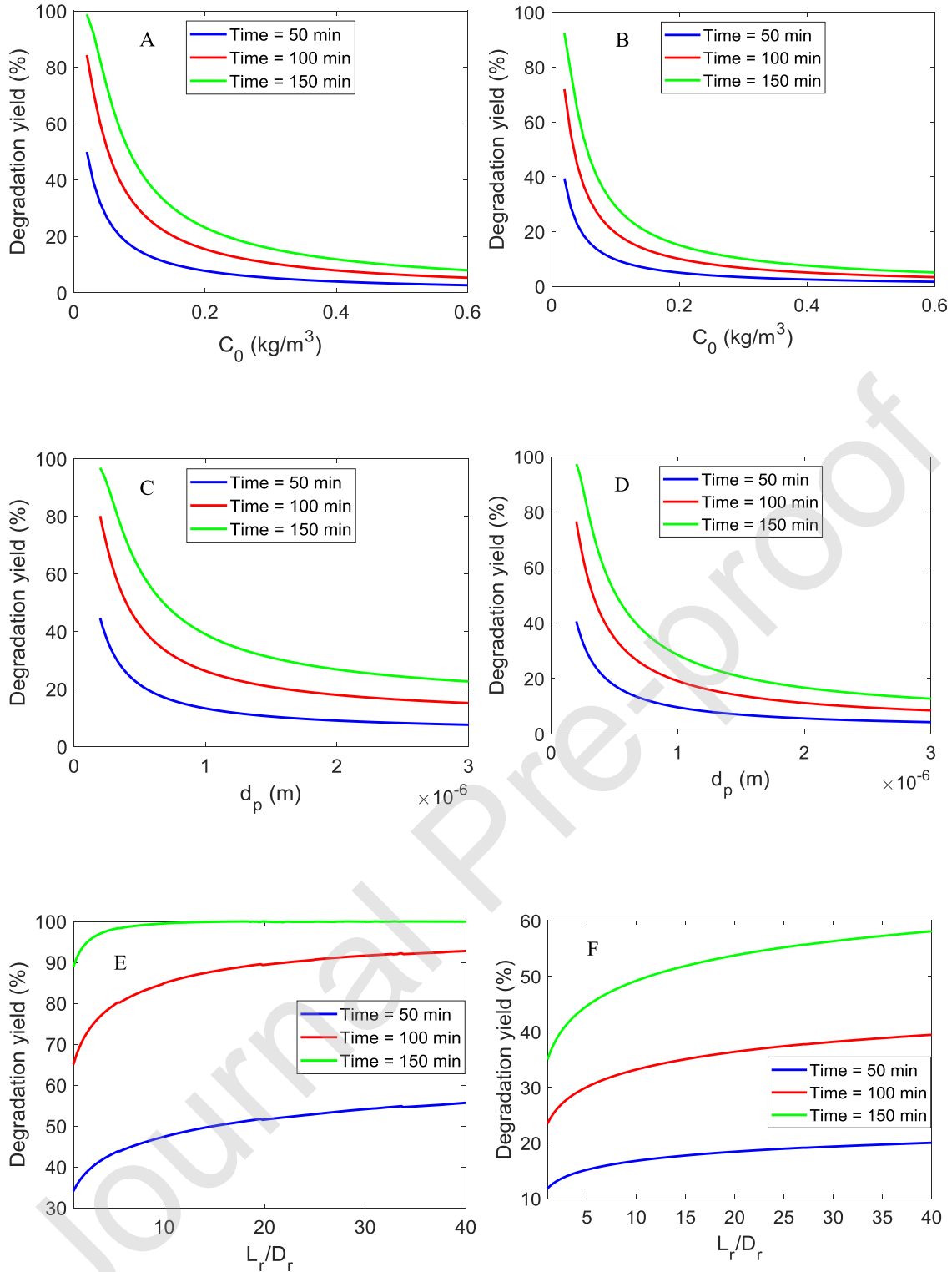| Dyes	Catalyst type	m_s (kg/m^3)	C_0 (kg/m^3)	t (min)	Power (W)	Wave (nm)	Max. Degradation (%)	Ref.
MO	PG-ZnO	0.50	0.013	150	-	Sun light	100	(Wang et al., 2019)
Paracetamol	Nd-V-ZnO	1.0	0.01	150	500	> 400	69.7	(Alam et al., 2019)
RBB	Co-ZnO	1.0	0.02	120	130(*)	320-400	91.4	(Tani et al., 2019)
MG	Cu-ZnO	0.40	0.03	80	58	> 400	88.7	(Modwi et al., 2019)
AY99	Ag-ZnO	0.60	0.03	60	-	280–100	92.6	(El-Bindary et al., 2019)
Blue-199	Ct-ZnO	0.33	0.05	90	-	UV-sun light	43.8	(Ali et al., 2018)
MB	ZnO	0.50	0.01	80	30	400	90	(Yu et al., 2019)
RB 19	ZnO	0.8	0.05	25	125	>254	90	(Lizama et al., 2002)
RB 21	ZnO	0.667	0.2	270	400	250	90	(Davar et al., 2015)
RB 21	ZnO	0.6	0.04	240	250	250	80.3	(Wang et al., 2019)

* Units in W/m^2

31

Table 2 - Chemicals composition of the effluent.

Chemicals Amount				Function	
A	Sodium Hydroxide	1.40	(g L⁻¹)	Increase of pH and saponification of oil and waxes	
	Nonionic Detergent	1.00		Emulsification of oil and waxes	
	Sodium Metasilicate	0.50		Peroxide Stabilizer	
	Levelling Agent	1.00	(mL L⁻¹)	Dispersion of hardness salts	
	Hydrogen Peroxide	2.00		Bleaching agent	
B	Sulfuric Acid	0.14	(mL L⁻¹)	To attain a pH of 6.5	
C	Catalase Enzime	0.50	(g L⁻¹)	Removal peroxide residual	
D	RB19 and RB21	1,5 %	on weight of material	Dyestuffs	
E	Sodium Hydroxide	1.40	(g L⁻¹)	Ionization of the cellulose hydroxyl groups	
	Sodium Carbonate	5.0			
	Sodium Chloride	50.00		Minimize electromagnetic repulsion between fiber/dyestuff	
F	Sulfuric Acid	0.14	(mL L⁻¹)	To attain a pH of 6.5	
G	Levelling Agent	0.50	(mL L⁻¹)	To remove hydrolysed dyestuff	

Table 3 – Numerical values of the model parameters.

Parameter	Unit		Numerical value	
			RB21	RB19
$k_{rxn}I\times10^3$	1/s		2.2	0.98
$R_{phot}\times10^7$	kg/m^3.s		8.019	29.21
$q_{max}\times10^7$	kg/m^2		4.081	12.533
$b\times10^{-2}$	m^3/kg		1.959	0.95
$C_0\times10^2$	kg/m^3		5.853	7.059
$d_p\times10^7$	m		5.471	
$D_l\times10^2$	m		1.9	
$D_r\times10^2$	m		3.7	
$D_e\times10^2$	m		1.596	
$L_l\times10^1$	m		2.88	
$L_r\times10^1$	m		2.88	
$L_e\times10^0$	m		1.86	
$a\times10^{-3}$	1/m		9.162	
$U_r\times10^2$	m/s		2.072	
$U_e\times10^2$	m/s		8.2	

Table 4 - Comparison total photocatalytic degradation in present study and relevant publications

Dyes	Catalyst type	m_s (kg/m^3)	C_0 (kg/m^3)	t (min)	Power (W)	Wave (nm)	Max. Degradation (%)	Ref.
Pure-RB 21	TiO_2	0.01	0.12	120	15	250-320	93	(Bahreini et al., 2016)
Pure-RB 21	Ag_3PO_4-$BiPO_4$	0.01	0.01	120	125	250-700	93	(Mohaghegh et al., 2015)
Pure-RB 21	$MgMn_2O_4$	0.6	0.02	60	90	> 400	95	(Moradnia et al., 2019)
Pure-RB 21	$NiFe_2O_4$-ZnO	1.6	0.05	240	-	250	80	(Pardiwala et al., 2016)
Pure-RB 21	$NiFe_2O_4$@ZnO MNCs	1.4	0.02	60	80	> 400	96	(Moradi et al., 2018)
Pure-RB 21	V_2O_5	0.5	0.025	60	30 (*)	250	97	(Al-Anbari et al., 2017)
Pure-RB 21	$Zn_{0.5}Ni_{0.5}AlFeO_4$MNPs	0.6	0.02	60	90	> 400	94	(Atrak et al., 2019)
Pure-RB 21	$MgFe_2O_4$ MNPs	0.1	0.1	180	80	> 400	95	(Fardood et al., 2017)
Pure-RB 21	ZnO-NPs	0.667	0.2	270	400	250	90	(Davar et al., 2015)
Effluent-RB 21	ZnO	1.667	0.07	360	7.1	250-700	91	This paper
Effluent-RB 19	ZnO	1.667	0.07	360	7.1	250-700	100	This paper
Pure-RB 19	ZnO-SiO_2	0.8	0.025	240	150	300-400	85.9	(Maučec et al., 2018)
Pure-RB 19	PANI-TiO_2	1	0.05	120	36	250	98.4	(Kalikeri et al., 2018)
Pure-RB 19	S-TiO_2	0.2	0.02	120	200	400-700	23	(Khan et al., 2015)
Pure-RB 19	$BiVO_4$-coated	2.5	0.015	70	400	> 420	94	(Khan et al., 2015)
Pure-RB 19	PDA-Ag-WO_3	-	0.05	180	1000	400	97.8	(Fan et al., 2019)
Pure-RB 19	$BiVO_4$/Bi_2WO_6	-	-	120	1000	> 420	95	(Lin et al., 2016)
Pure-RB 19	Bi_2MoO_6/Ag/AgCl	0.6	0.05	120	1000	400	95	(Yang et al. 2019)

* Units in W/m^2